Segregation Tendency in Layered Aluminum-Substituted Lithium Nickel Oxides

L. Croguennec,*[,†,‡] Y. Shao-Horn,[†,‡,§] A. Gloter,[#] C. Colliex,[#] M. Guilmard,[†,‡] F. Fauth,[⊥,||] and C. Delmas[†,‡]

CNRS, ICMCB, 87 avenue Dr A. Schweitzer, 33608 Pessac cedex, Université de Bordeaux, ICMCB, ENSCPB, 33608 Pessac cedex, France, Laboratoire de Physique des Solides, Université Paris-Sud, Bâtiment 510, 91405 Orsay cedex, France, and European Synchrotron Radiation Facility (ESRF), BP 220, 6, Rue Jules Horowitz, 38043 Grenoble, France

Received October 29, 2008. Revised Manuscript Received January 14, 2009

Conventional X-ray powder diffraction analyses of aluminum-substituted lithium nickel oxides showed pronounced broadening of the (11*l*) type peaks with increasing aluminum concentrations. It was postulated that a segregation tendency of nickel and aluminum in the layered lithium nickel oxide structure could lead to anisotropic strains and size effects for the (110) type planes and thus pronounced broadening. Variation in the distribution of aluminum and nickel was detected among different crystals by energy-dispersive X-ray spectroscopy (EDX) and within individual crystals at the nanometer-scale by electron energy loss spectroscopy (EELS). Synchrotron X-ray powder diffraction analyses of the "$LiNi_{1-y}Al_yO_2$" ($0.10 \leq y \leq 0.50$) samples revealed that strains in the (110) planes continuously increased with the aluminum concentration, which was then confirmed by convergent beam and selected area electron diffraction studies. Therefore, a combination of synchrotron X-ray powder diffraction, electron diffraction, EDX, and EELS analyses provided, for the first time, direct evidence for the segregation tendency of nickel and aluminum in the layered lithium nickel oxide structure, from which a domain microstructure for the "$LiNi_{0.50}Al_{0.50}O_2$" sample was proposed.

Introduction

Aluminum substitution in layered lithium nickel oxides ("$LiNi_{1-y}Al_yO_2$") has been shown to have several positive effects in the development of positive electrode materials for lithium rechargeable batteries: (1) increasing average lithium intercalation and deintercalation voltages,[1−5] (2) enhancing the thermal stability of lithium deintercalated compounds[6,7] and thus lithium battery safety,[8,9] and (3) improving lithium battery cycle life[9−11] at the expense of the reversible capacity. In general, "$LiNiO_2$" with a chemical formula of $Li_{1-z}Ni_{1+z}O_2$ is isostructural to α-$NaFeO_2$ with space group $R\bar{3}m$, having 1Ni in the 3*a* site, (1−*z*)Li and *z*Ni in the 3*b* site, and 2O ions in the 6*c* site. The comparison of the X-ray diffraction patterns of "$LiNi_{1-y}Al_yO_2$" as a function of *y* shows that at low concentrations of aluminum substitution (<0.15) in the layered $LiNiO_2$ structure, a $Li(Ni,Al)O_2$ solid solution appears to be achieved,[11−14] where nickel and aluminum ions are randomly distributed on the 3*a* sites. However, at higher concentrations of aluminum substitution (≥0.15), although the layered "$LiNi_{1-y}Al_yO_2$" (α-$NaFeO_2$ structure type) structure with space group $R\bar{3}m$ remains to be the major phase, some aluminum-rich phases such as γ-$LiAlO_2$ and β-Li_5AlO_4 are present as minor impurities. This results in the fact that the major phase in the "$LiNi_{0.50}Al_{0.50}O_2$" sample has a Ni/Al ratio greater than 1. In addition, although some peak broadening was observed for all the reflections upon increasing aluminum substitution, X-ray diffraction (XRD) peaks such as the (11*l*)-type have shown to be pronouncedly broadened,[11] as highlighted in

* Corresponding author. Phone: 33-5-4000-2234 (or 2647). Fax: 33-5-4000-6698. E-mail: laurence.croguennec@icmcb-bordeaux.cnrs.fr.
† CNRS, ICMCB.
‡ Université de Bordeaux, ICMCB, ENSCPB.
§ Present address: Department of Mechanical Engineering and Department of Materials Science and Engineering, Massachusetts Institute of Technology, Cambridge, MA 02139.
# Université Paris-Sud.
|| European Synchrotron Radiation Facility.
⊥ Present address: BM16-CRG/Consorci Laboratori Llum Sincrotro (LLS) c/o European Synchrotron Radiation Facility (ESRF), BP 220/6, rue Jules Horowitz, F-38043 Grenoble, France.

(1) Aydinol, M. K.; Kohan, A. F.; Ceder, G.; Cho, K.; Joannopoulos, J. *Phys. Rev. B* **1997**, *56*, 1354–1365.
(2) Ceder, G.; Chiang, Y. M.; Sadoway, D. R.; Aydinol, M. K.; Jang, Y. I.; Huang, B. *Nature* **1998**, *392*, 694–666.
(3) Jang, Y. I.; Huang, B. Y.; Wang, H. F.; Sadoway, D. R.; Ceder, G.; Chiang, Y. M.; Liu, H.; Tamura, H. *J. Electrochem. Soc.* **1999**, *146*, 862–868.
(4) Ohzuku, T.; Nakura, K. *Denki Kagaku* **1998**, *66*, 1209–1214.
(5) Ohzuku, T.; Nakura, K.; Aoki, T. *Electrochim. Acta* **1999**, *45*, 151–160.
(6) Guilmard, M.; Croguennec, L.; Denux, D.; Delmas, C. *Chem. Mater.* **2003**, *15*, 4476–4483.
(7) Guilmard, M.; Croguennec, L.; Delmas, C. *Chem. Mater.* **2003**, *15*, 4484–4493.
(8) Ohzuku, T.; Ueda, A.; Kouguchi, M. *J. Electrochem. Soc.* **1995**, *142*, 4033–4039.
(9) Ohzuku, T.; Yanagawa, T.; Kouguchi, M.; Ueda, A. *J. Power Sources* **1997**, *68*, 131–134.
(10) Park, S. H.; Park, K. S.; Sun, Y. K.; Nahm, K. S.; Lee, Y. S.; Yoshio, M. *Electrochim. Acta* **2001**, *46*, 1215.
(11) Guilmard, M.; Rougier, A.; Grüne, A.; Croguennec, L.; Delmas, C. *J. Power Sources* **2003**, *115*, 305–314.
(12) Zhong, Q.; Von Sacken, U. *J. Power Sources* **1995**, *54*, 221.
(13) Wang, G. X.; Zhong, S.; Bradhurst, D. H.; Dou, S. X.; Liu, H. K. *Solid State Ionics* **1999**, *116*, 271–277.
(14) Rougier, A. Ph.D. Dissertation, Université de Bordeaux I, Bordeaux, France, 1995.

10.1021/cm802954g CCC: $40.75
Published on Web 02/12/2009

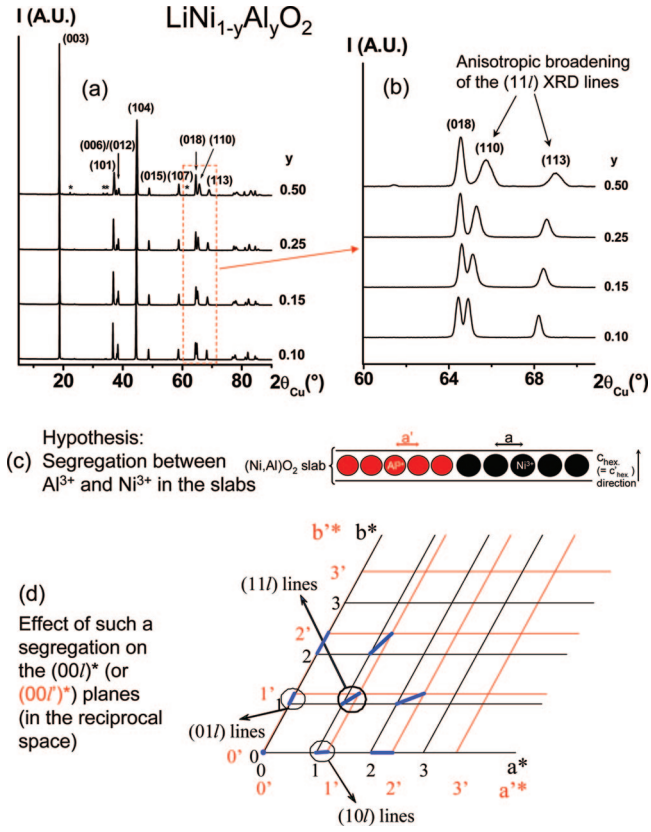

Figure 1. (a, b) Experimental X-ray powder diffraction patterns of the "$LiNi_{1-y}Al_yO_2$" samples ($y = 0.10-0.50$) with Cu Kα radiation ($\lambda_{K\alpha 1}$ = 1.5406 Å) and enlargement of the 60−71°2θ range in order to clearly reveal the anisotropic broadening of the (11l) lines that could be associated to Ni^{3+}/Al^{3+} segregation in the slabs. (c) The effect of such a cation segregation is schematically explained, considering (d) a representation in the same reciprocal space of the lattices associated with Al-rich ((a'^*, b'^*, $c'^* \cong c^*$) in red) and Ni-rich ((a^*, b^*, $c^* \cong c'^*$) in black) domains. Local variations (Δd_{hkl}) in the d_{hkl} distances lead to the broadening and displacement of the diffraction lines affected by the strains. As highlighted by the blue segments (−), those increase with $h+k$.

panels a and b in Figure 1. Such anisotropic broadening differs from isotropic broadening in that it does not increase monotonically with the diffraction angle. Similar broadening of the (11l)-type diffraction lines were observed by other authors for high concentrations of aluminum substitution.[4,5] Such broadening cannot be explained adequately by considering a mixture of multiple $LiNi_{1-y}Al_yO_2$ phases that are close in composition in the sample. In general, such anisotropic broadening can be attributed to (1) anisotropic crystal size, (2) anisotropic strains, or (3) stacking faults in the parent structure.

Aluminum substitution considerably modifies the lattice parameter $a_{hex.}$ of the layered structure but only slightly changes the lattice parameter $c_{hex.}$.[11] Considering the difference in electronegativity ($\chi(Ni^{3+}) = 1.91$ and $\chi(Al^{3+}) = 1.61$) between Ni^{3+} and Al^{3+}, that show rather similar ionic radii ($r_i(Ni^{3+}) = 0.56$ Å and $r_i(Al^{3+}) = 0.53$ Å), it is proposed in this study that they may segregate in the basal planes of the layered structure, as shown in Figure 1c. There would be a distribution of metal−metal distances in the slabs (i.e., in the ($a_{hex.}$, $b_{hex.}$) plane), those being equal to a' in Al-rich domains and to a in Ni-rich domains. As the $c_{hex.}$ lattice parameter is only slightly affected by the aluminum substitution for nickel, the representation of the reciprocal lattices associated with Al-rich ((a'^*, b'^*, $c'^* \cong c^*$) in red) and Ni-rich ((a^*, b^*, $c^* \cong c'^*$) in black) domains in the same reciprocal space is possible. Such cation segregation can lead to local variations (Δd_{hkl}) in the d_{hkl} distances and thus to broadening and displacement of the diffraction lines affected by the strains among Ni- and Al-rich domains. With this hypothesis, the broadening of the diffraction lines is clearly anisotropic and proportional to the length of the blue segments in the reciprocal space shown in Figure 1d having broadening increasing with $h+k$.

The proposed nickel and aluminum segregation in the "$LiNi_{1-y}Al_yO_2$" system is in apparent conflict with first-principles calculations, which show a $Li(Al,Ni)O_2$ solid solution expected at room temperature.[16] Buta et al. have considered for "$LiNi_{1-y}Al_yO_2$" materials used for these first-principles studies[16] that aluminum and nickel ions were ordered in the slabs and that the packing was strictly lamellar. However, experimentally obtained "$LiNi_{1-y}Al_yO_2$" samples ($0.10 \leq y \leq 0.50$) show no cation ordering in the slabs and ~5% excess of Ni^{2+} ions in the lithium layers.[11] Such discrepancies in the structure and the cation distribution could lead to substantially different results in the predicted phase diagram of $Li(Al,Ni)O_2$[16] from actual materials.

In this study, we probe the nature of selective peak broadening observed in the XRD patterns of '"$LiNi_{1-y}Al_yO_2$" samples and determine whether segregation of nickel and aluminum exists in the layered "$LiNi_{1-y}Al_yO_2$" structure. Here we combine synchrotron XRD analysis and single-crystal electron diffraction with high spatial resolution (from the micrometer to the nanometer scale) to study the layered "$LiNi_{1-y}Al_yO_2$" structure substituted with different aluminum concentrations. As synchrotron X-ray powder diffraction can provide peak shapes intrinsic to the samples in contrast to conventional X-ray powder diffraction with significant instrumental broadening, it is used to study anisotropic strain effects in the "$LiNi_{1-y}Al_yO_2$" samples as a function of the aluminum content. In addition, smaller wavelengths of synchrotron radiation allow collection of diffraction data in larger ranges of interplanar spacing relative to conventional X-ray sources. Moreover, we study and map the distributions (or chemical inhomogeneity) of nickel and aluminum ions in the "$LiNi_{1-y}Al_yO_2$" samples 1) from crystals to crystals using backscattered electron imaging and energy-dispersive spectroscopy in the scanning electron microscope and electron energy loss spectroscopy (EELS) in the transmission electron microscope and 2) within individual crystals using EELS. Structural and chemical information of layered "$LiNi_{1-y}Al_yO_2$" samples ($0.10 \leq y \leq 0.50$) from the micrometer to the nanometer-scale will be coupled to provide insights into the nature of nickel and aluminum arrangements in the layered lithium nickel oxide structure, particularly at high aluminum concentrations (with $y \geq 0.25$).

Experimental Section

Aluminum substituted lithium nickel oxide samples with nominal compositions of "$LiNi_{1-y}Al_yO_2$" ($y = 0.10, 0.15, 0.25, 0.50$) were

(15) Poeppelmeier, K. R.; Chiang, C. K.; Kipp, D. O. *Inorg. Chem.* **1988**, *27*, 4523–4524.
(16) Buta, S.; Morgan, D.; Vanderven, A.; Aydinol, M. K.; Ceder, G. *J. Electrochem. Soc.* **1999**, *146*, 4335–4338.

prepared by a solution−precipitation process as described previously[11,17] and followed by heat treatments at 700 or 750 °C in an oxygen stream for 5−15 h. These "$LiNi_{1-y}Al_yO_2$" samples were first analyzed by conventional X-ray powder diffraction with Cu Kα on a Siemens D5000 diffractometer. The lattice and structural parameters of "$LiNi_{1-y}Al_yO_2$" were obtained from the Rietveld refinement of the experimental X-ray powder diffraction patterns[11] collected at a step size of 0.02° and a step time of 40 s with the Fullprof software package.[18]

To examine whether nickel and aluminum ions were distributed uniformly on the micrometer scale, we performed backscattered electron (BSE) imaging on the metallographically polished surfaces of a pressed "$LiNi_{0.50}Al_{0.50}O_2$" pellet sample in a LEO scanning electron microscope under an accelerating voltage of 20 KeV. Energy-dispersive X-ray (EDX) spectra of the polished surfaces were collected and used to determine the average nickel and aluminum concentrations of different crystals. Quantitative analyses of nickel and aluminum concentrations were conducted by comparing the Ni *L* and Al *K* peak intensities collected at an accelerating voltage of 10 KeV using LEO correction software and ZAF correction algorithms to correct for interferences between elements, source of errors in quantitative microanalyses.

The synchrotron X-ray powder diffraction patterns of "$LiNi_{1-y}Al_yO_2$" samples ($y = 0$, 0.10, 0.15, 0.25, and 0.50) were collected on the powder diffraction beamline BM16 of the European Synchrotron Radiation Facilities (ESRF, Grenoble, France). The powder samples placed in quartz ($y = 0$, 0.15 and 0.50) or glass ($y = 0.10$ and 0.25) capillaries were characterized by X-rays with a wavelength of 0.30964 Å and of 0.49630 Å, respectively. All synchrotron diffraction data were collected at room temperature with a final effective step of 0.003° (2θ) and refined with the Rietveld method using the program Fullprof and the Winplotr interface.[18] To obtain isotropic strain and size parameters required for the "Thompson−Cox−Hastings pseudo-Voigt" profile function, a "$LiNiO_2$" powder sample was used as a standard for the Rietveld refinement of all the synchrotron diffraction data of the "$LiNi_{1-y}Al_yO_2$" samples. We assumed that the "$LiNiO_2$" sample had no anisotropic size and strain effect and we only refined the Gaussian (*U*) and Lorentzian (*X*) parameters of the isotropic strain component and the Lorentzian parameter (*Y*) of the isotropic size component. Parameter *W* was fixed to the instrumental broadening of 7×10^{-5}; the Gaussian parameter (IG) of the isotropic size component was set to zero, as it was found to be not significant to the refinement results. A good agreement was obtained between the experimental and calculated XRD patterns of "$LiNiO_2$" with reliability factors R_{Bragg} of 1.14% and Rwp 14.6% and these refined parameters, *U*, *X*, and *Y*, converged to 0.012, 0.060, and 0.0047, respectively. Having these parameters fixed, a general model described by P.W. Stephens[19] was used to quantify anisotropic strains (Γ_A). Those are function of the variance $\sigma[1/(d_{hkl})^2]$ that reflects the distribution of the distances between lattice planes in a given network and are expressed as $\Gamma_A = [\sigma^2(1/(d_{hkl})^2)]^{1/2}\tan\theta/(1/(d_{hkl})^2)$. The variance $\sigma[1/(d_{hkl})^2]$ is itself defined as $\sigma^2(1/(d_{hkl})^2) = \Sigma S_{HKL}h^Hk^Kl^L$ with $H + K + L = 4$. In the most general system, i.e., the triclinic system, 15 independant S_{HKL} parameters are required to describe the anisotropic strain model. The mixing factor ξ allows for assigning an anisotropic broadening term, $\xi\Gamma_A$ and $(1-\xi)\Gamma_A$, to the Lorentzian and Gaussian parts of the profile function respectively. In the present case (i.e., trigonal symmetry in the hexagonal cell setting), only four S_{HKL} independent parameters (S_{400}, S_{004}, S_{112}, and S_{211}) and the mixing factor ξ were required to describe the anisotropic strain model.

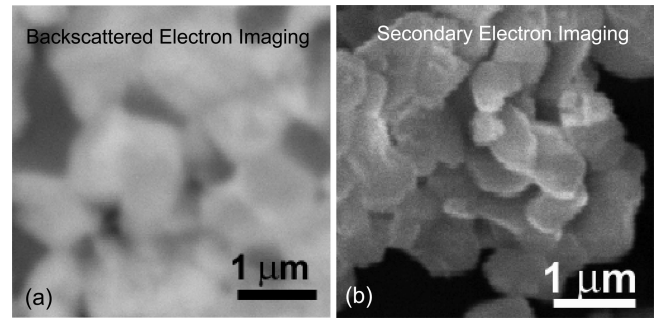

Figure 2. (a) Backscattered electron imaging of metallographically polished surfaces of a pressed "$LiNi_{0.50}Al_{0.50}O_2$" pellet sample, which reveals primary crystal sizes on the order of 0.5−1 μm and (b) secondary electron imaging of loose "$LiNi_{0.50}Al_{0.50}O_2$" particles.

Selected area and convergent beam electron diffraction patterns were collected from the "$LiNi_{1-y}Al_yO_2$" powder suspended on a copper grid with lacey carbon under an accelerating voltage of 200 KeV on a JEOL 2000FX transmission electron microscope. Energy-dispersive X-ray (EDX) spectra were collected and used to determine the average nickel and aluminum concentration of individual crystals.

EELS spectra were collected from different crystals and different regions within individual crystals of the "$LiNi_{0.50}Al_{0.50}O_2$" sample using (1) a Gatan CCD modified 666 PEELS device on a VG HB 501 STEM with a field emission gun and a working accelerating voltage of 100 KeV and (2) a Gatan CCD modified 666 PEELS device on a Topcon CTEM with a LaB_6 electron gun and a working accelerating voltage of 200 KeV. Elemental EELS quantification was performed using a conventional smooth power law extrapolation under the Ni $L_{2,3}$ and Al *K* edges and cross-sections calculated within a Hartree-type model with white lines correction.

Results and Discussions

Scanning Electron Microscopy Analysis. As shown in Figure 2a, backscattered electron imaging of the metallographically polished surface of a pressed "$LiNi_{0.50}Al_{0.50}O_2$" pellet sample clearly revealed primary crystal sizes on the order of 0.5−1 μm, but also heterogeneity in composition between these primary crystals. Indeed, as the contrast in the backscattered electron images reflects differences in the average atomic number, the aluminum-rich impurities γ-$LiAlO_2$ and β-Li_5AlO_4 could be easily identified as dark regions in Figure 2a. The size and morphology of loose "$LiNi_{0.50}Al_{0.50}O_2$" particles are shown in a secondary electron image in Figure 2b for comparison. EDX analysis in scanning electron microscopy was then used to determine the average relative percentages of nickel and aluminum of the dark and bright zones in the backscattered electron images. As the Ni L peak is closer to the Al K peak in energy than the Ni K peak, the Ni L and Al K peaks were used in the quantification in order to minimize the errors introduced by the ZAF correction. The relative percentages of nickel and aluminum analyzed from eight different locations of the polished "$LiNi_{0.50}Al_{0.50}O_2$" pellet sample are plotted in Figure 3. The dark zones were found to be aluminum-rich with an average Ni/Al ratio about equal to 1/9. The bright zones were found to be nickel-rich with an average Ni/Al ratio equal to 0.57/0.43, which supports, by comparison with other $Li_{1-z}Ni_{1+z}O_2$

(17) Caurant, D.; Baffier, N.; Garcia, B.; Pereira-Ramos, J. P. *Solid State Ionics* **1996**, *91*, 45–54.
(18) Rodriguez-Carvajal, J. *J. Physica B* **1993**, *192*, 55.
(19) Stephens, P. W. *J. Appl. Crystallogr.* **1999**, *32*, 281–289.

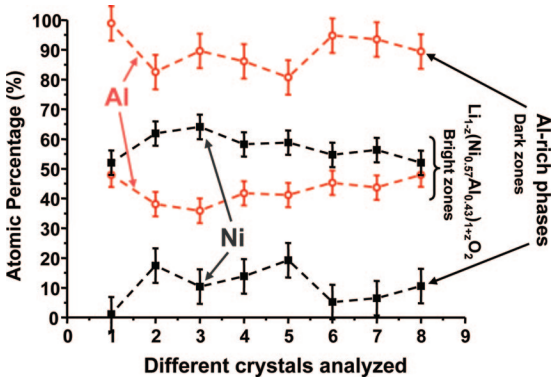

Figure 3. Relative nickel and aluminum percentages of different crystals (regions) from the metallographically polished "$LiNi_{0.50}Al_{0.50}O_2$" specimen determined from EDX analysis in the scanning electron microscope.

and $Li_{1-z}(Ni, Al)_{1+z}O_2$ compounds studied earlier, an average chemical composition of $Li_{1-z}(Ni_{0.57}Al_{0.43})_{1+z}O_2$ and thus the presence of aluminum-rich phases as impurities and a Ni/Al ratio larger than $1-y/y$ for the α-$NaFeO_2$ type phases.[11] As the activation volume of Al K X-rays is on the order of 1 μm^3 for an accelerating voltage of 10 KeV, overlapping of bright and dark regions within the activation volume in the direction perpendicular to the polished sample surface affects the relative percentages of nickel and aluminum in the bright and dark regions. Nevertheless, variation in the distribution of nickel and aluminum was detected among different crystals; this variation, as will be discussed in the following, was also detected by EELS that on the contrary to EDX shows an activation volume much smaller than the crystals' size.

Synchrotron X-ray Powder Diffraction Analysis. The size and strain effects in the different "$LiNi_{1-y}Al_yO_2$" samples were qualitatively evaluated by constructing Williamson-Hall plots (FWHM cosθ vs sinθ)[20] from the synchrotron X-ray powder diffraction data, those confirmed an increase in the anisotropic broadening of the diffraction lines with the increasing aluminum concentration in the $LiNi_{1-y}Al_yO_2$ samples. The Williamson−Hall plot obtained for "$LiNi_{0.50}Al_{0.50}O_2$" is given as an example in Figure 4. It clearly reveals the anisotropic broadening of the lines with 2θ. As highlighted by the gray zones on the plot the larger the $(h+k)$ value, the broader the diffraction line. Furthermore, as shown by the dotted lines, the slope (i.e., the strains) of FWHM cos θ vs sin θ was shown to increase for the (012) and (104) crystallographic planes in comparison with that for the (003) crystallographic planes. Strains in the (003) planes were thus found to be much smaller than those in the (012) and (101) planes. In addition, the reciprocal of the intercept (i.e., the isotropic size) for the (003) crystallographic planes was found to be large for all samples, which implied no significant size effects in the direction perpendicular to the (003) planes with an increasing aluminum substitution for nickel. For instance, a coherent domain size of ∼4000 Å along this direction was found in the "$LiNi_{0.50}Al_{0.50}O_2$" sample. Similar results were obtained for the (012) and (104) planes. As nickel and aluminum segregation leads to spatial fluctuations of the metal−metal distances in the slabs,

(20) Williamson, G. K.; Hall, W. H. *Acta Metall.* **1953**, *1*, 22–31.

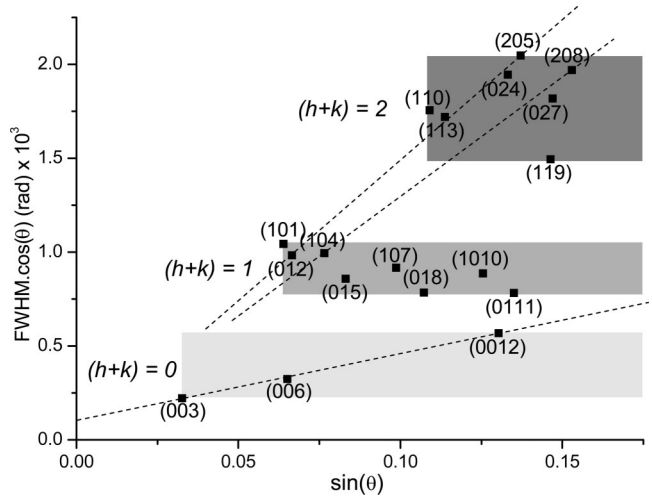

Figure 4. Williamson−Hall plot[20] constructed for "$LiNi_{0.50}Al_{0.50}O_2$" from synchrotron X-ray diffraction data. This analysis is based on the fact that the broadening due to lattice strains and that due to size have a different angular dependence: FWHM $(\cos\theta/\lambda) = 1/D + K\varepsilon(\sin\theta/\lambda)$, where FWHM is the full width at half-maximum, λ the wavelength, D the size of the coherently diffracting domains, ε the lattice strains, and K is a constant close to 1 that mainly depends on the crystallite morphology and on the definition taken for the line width. The gray zones highlight the increasing broadening of the (hkl) lines with the value of $(h+k)$, whereas the dotted lines show that for the (003), (012), and (104) crystallographic planes, the strains increase with the value of $(h+k)$.

maximum strain and/or size effects would thus be expected in the (110) planes. Unfortunately, as only one reflection order was available for the (110) and (113) crystallographic planes in the scan range collected, we could not distinguish if there were anisotropic strains only, anisotropic size effects only or combination of both in the "$LiNi_{1-y}Al_yO_2$" samples.

Although anisotropic strain and size effects are expected to be highly correlated in the slabs, we here use the Rietveld refinement analysis to quantify the strains only, as attempts to introduce any anisotropic size effects have led to poor reliability factors and minimization of the difference between $I_{exp.}$ and $I_{calc.}$. Refinements of these synchrotron X-ray diffraction data were realized assuming for "$LiNi_{1-y}Al_yO_2$" an α-$NaFeO_2$-type structure (described in the $R\bar{3}m$ space group) characterized by the cationic distribution $[Li_{1-z}Ni^{II}_z]_{3b}[Ni^{III}_{1-t-z}Ni^{II}_zAl_t]_{3a}O_2$ (t being equal to $y(1-z)$). This model was previously proposed by some of us to describe the structure of '"$LiNi_{1-y}Al_yO_2$" according to X-ray and neutron diffraction analyses as well as magnetic measurements.[11] The site occupancies were constraint to be equal to 1 with $(1-z)$Li and zNi in the 3b (0,0,1/2) site, $(1-t)$Ni and tAl in the 3a (0,0,0) site and 1 O in the 6c (0,0,$z_{ox.}$) site ($z_{ox.}$ being close to 1/4). z value was refined and t was constraint to be equal to $y(1-z)$. The isotropic atomic displacement parameters (B) were allowed to vary but were constraint to be equal for atoms sitting in the same site. The profile function was defined as largely described in the experimental part of this paper. Comparison between experimental and calculated patterns, obtained for those latter considering a structural model with or without anisotropic strains, are given in Figure 5 for "$LiNi_{0.50}Al_{0.50}O_2$". As shown by this comparison, the matching between the experimental and calculated patterns of the "$LiNi_{1-y}Al_yO_2$" samples was significantly improved by considering anisotropic strain

Table I. Structural and Microstructural Parameters Obtained for the "$LiNi_{1-y}Al_yO_2$" Samples from the Rietveld Refinement of Synchrotron X-ray Powder Diffraction Data Using a General Model to Describe Anisotropic Strain Broadening[19,a]

	"$LiNiO_2$"	"$LiNi_{0.90}Al_{0.10}O_2$"	"$LiNi_{0.85}Al_{0.15}O_2$"	"$LiNi_{0.75}Al_{0.25}O_2$"	"$LiNi_{0.50}Al_{0.50}O_2$"
$a_{hex.}$ (Å)	2.87723(6)	2.87501(3)	2.86973(6)	2.86055(3)	2.84084(6)
$c_{hex.}$ (Å)	14.1900(6)	14.2175(2)	14.2249(4)	14.2371(2)	14.2572(4)
$z_{ox.}$	0.2591(9)	0.2589(3)	0.2593(6)	0.2592(2)	0.2599(3)
z	0.018(6)	0.057(3)	0.055(7)	0.039(3)	0.047(3)
S_{400}		5.3(2)	21(1)	33.1(9)	114(3)
S_{004}		0.0069(6)	0.006(1)	0.0056(6)	0.0035(9)
S_{112}		−0.07(3)		−0.32(6)	0.5(1)
S_{211}		3.9(3)	5(1)	5.0(6)	10(2)
ξ		0.26(2)	0.06(2)	0.19(1)	0.02(1)
R_B (%)	1.14	2.86	3.01	4.41	5.81
R_{wp} (%)	14.6	12.2	15.8	13.6	14.5

[a] Profile parameters fixed to the values obtained for "$LiNiO_2$": $U = 0.012$, $W = 7 \times 10^{-5}$, $X = 0.060$, and $Y = 0.0047$.

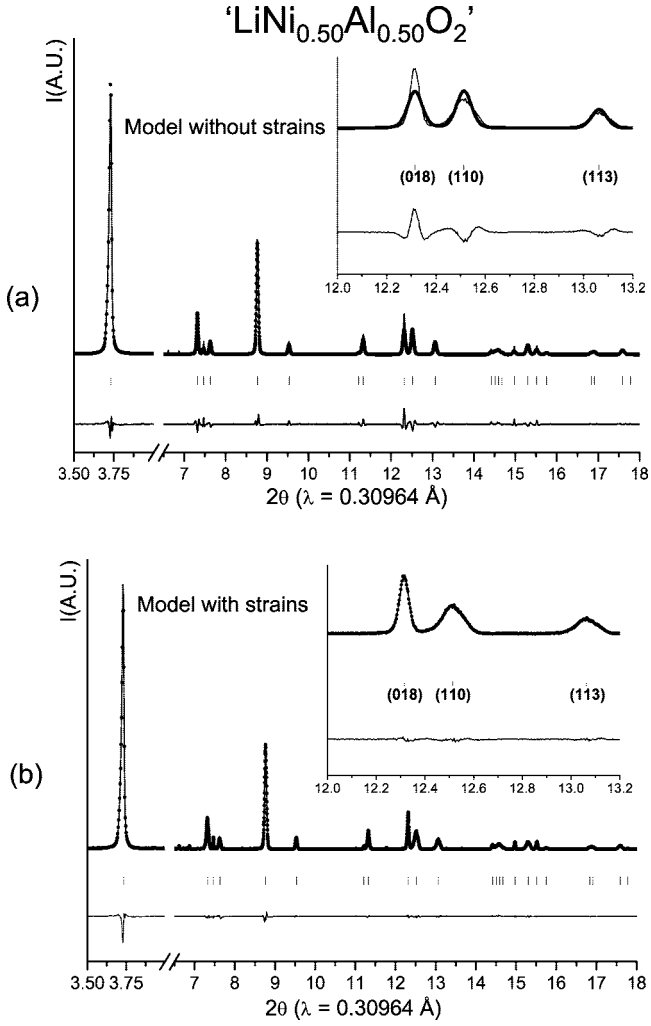

Figure 5. Comparison of calculated and experimental synchrotron XRD patterns of the "$LiNi_{0.50}Al_{0.50}O_2$" sample without (top panel) and with (bottom panel) considering strains in the layered structure. Zoomed regions in the 2θ range of 12.0−13.2° are compared on the right-hand side to show the (018), (110), and (113) peaks are much better refined with strain considerations.

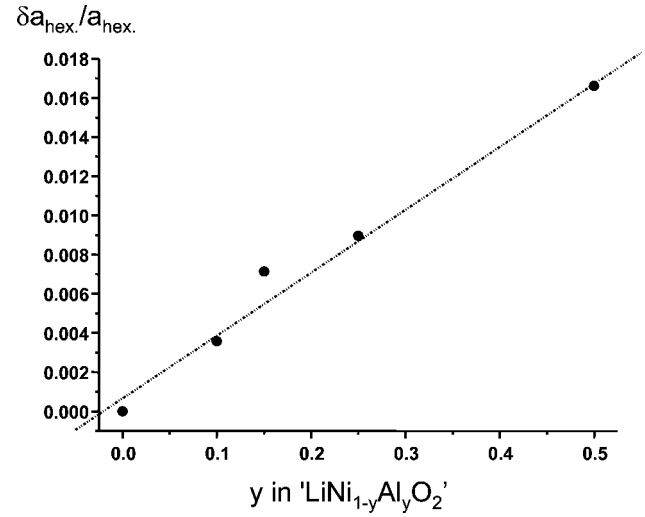

Figure 6. Plot of strains ε defined as $\delta a_{hex.}/a_{hex.}$ as a function of the aluminum content y in $LiNi_{1-y}Al_yO_2$. $\delta a_{hex.}/a_{hex.}$ is obtained from S_{400} (determined from the Rietveld analysis of the synchrotron X-ray diffraction patterns) through the formulas $\delta a_{hex.}/a_{hex.} = \pi d_{110}^2[20S_{400}]^{1/2}/18000$.[19]

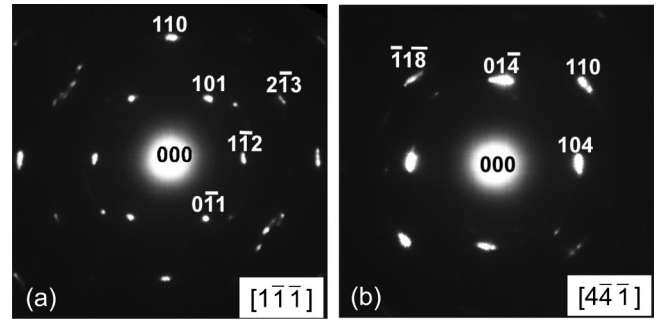

Figure 7. Single-crystal electron diffraction patterns collected from the "$LiNi_{0.50}Al_{0.50}O_2$" sample, which are indexed to (a) the $[1\bar{1}\bar{1}]$ and (b) $[4\bar{4}\bar{1}]$ zone axes of the layered structure with space group $R\bar{3}m$.

broadening. The structural, microstructural and profile parameters obtained for the "$LiNi_{1-y}Al_yO_2$" samples are given in Table I. The structural parameters ($a_{hex.}$, $c_{hex.}$, $z_{ox.}$, and z) are in agreement with those reported previously by some of us;[11] they show that substitution of aluminum for nickel results in shorter $a_{hex.}$ and larger $c_{hex.}$ as well as in the presence of about 0.05 divalent nickel ions in the lithium site. The small values of ξ are in good agreement with as expected a character mainly Gaussian for strains. In addition, S_{004} was found to be nearly zero for all the "$LiNi_{1-y}Al_yO_2$" samples, which confirmed the Williamson−Hall plot analysis in that strains along the $c_{hex.}$-axis ($\delta c_{hex.}/c_{hex.}$) were almost negligible. On the other hand, S_{400} was shown to increase with aluminum substitution for nickel. As shown in Figure 6, strains in the slabs ($\delta a_{hex.}/a_{hex.}$) increase with aluminum substitution for nickel.

Single-Crystal Electron Diffraction Analysis. Both selected area and convergent beam electron diffraction patterns were collected from the "$LiNi_{1-y}Al_yO_2$" ($y = 0.10$, 0.15, 0.25, 0.50) samples in order to understand the nature

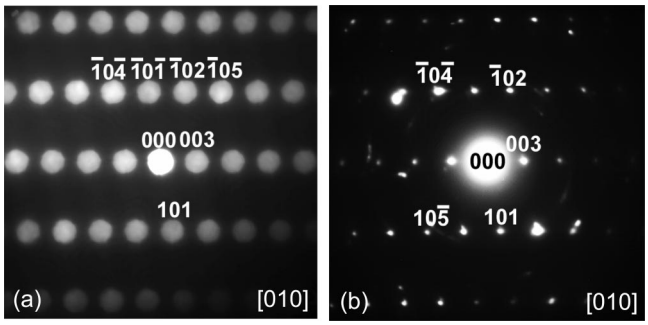

Figure 8. (a) [010] convergent beam electron diffraction and (b) selected area electron diffraction patterns collected from one crystal in the "$LiNi_{0.50}Al_{0.50}O_2$" sample.

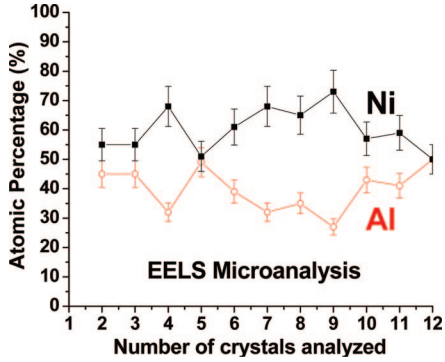

Figure 9. Relative nickel and aluminum percentages of several different crystals in the "$LiNi_{0.50}Al_{0.50}O_2$" sample determined from EELS spectra collected in the transmission electron microscope.

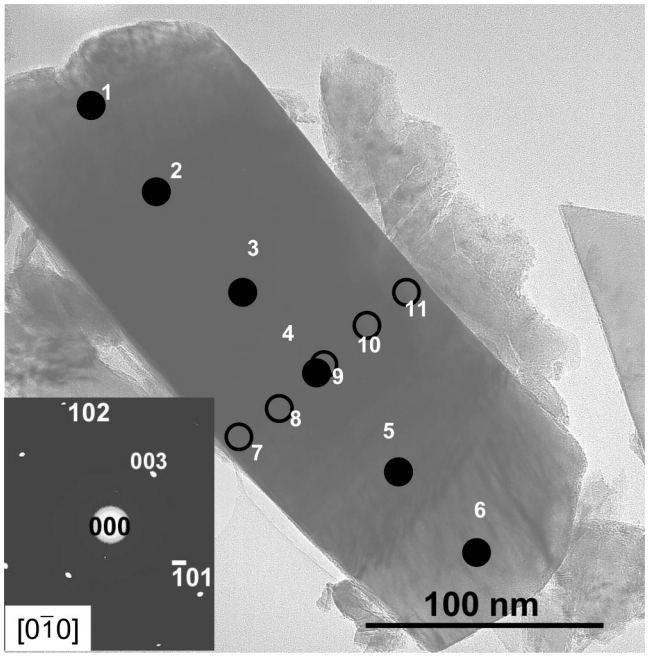

Figure 10. Transmission electron microscope image of a randomly selected "$LiNi_{0.50}Al_{0.50}O_2$" crystal and the diffraction pattern of this crystal shown in the insert (bottom left). EELS spectra were collected from 11 locations marked on the crystal.

of broadening of X-ray powder diffraction peaks. The presence of elastic strains - expansion and contraction of interplanar spacing, would lead to radial spreading of electron scattering intensities. Although some radial spreading was observed for selective diffraction reflections of "$LiNi_{1-y}Al_yO_2$" samples, the striking feature is the tangential smearing of

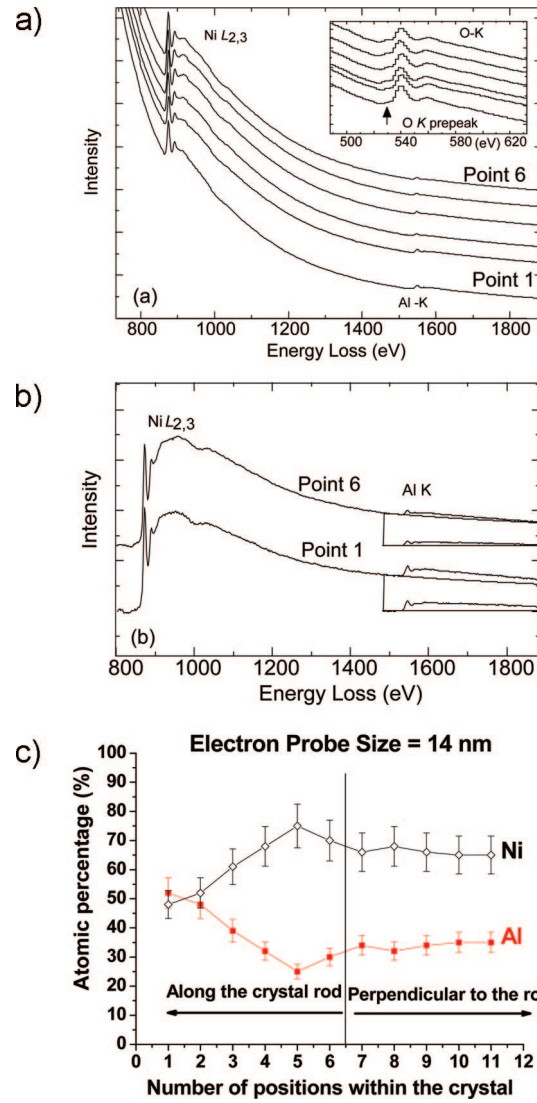

Figure 11. (a) EELS spectra of Ni $L_{2,3}$ and Al K peaks collected from point (location) 1 to point (location) 6 with the O K peaks collected from the same locations presented in the insert (top right); (b) Enlargement of EELS spectra of point 1 and point 6, which clearly shows a difference in the Al K peak intensity; (c) relative atomic percentages of aluminum and nickel in the crystal shown in Figure 10, which was quantified from the EELS spectra in (a) by comparing the peak intensities of the Ni $L_{2,3}$ and Al K peaks.

most electron diffraction spots which was found the most pronounced in the "$LiNi_{0.50}Al_{0.50}O_2$" sample. It should be noted that tangential smearing is associated with variation in the crystallographic orientation of atomic planes.

Two diffraction patterns collected from two different locations of a randomly selected and representative particle from the "$LiNi_{0.50}Al_{0.50}O_2$" sample are shown in panels a and b in Figure 7. They are indexed to the [$1\bar{1}\bar{1}$] and [$4\bar{4}\bar{1}$] zone axes of the rhombohedral layered structure with space group $R\bar{3}m$, respectively. The average chemical composition of the particle was $LiNi_{0.55}Al_{0.45}O_2$ as determined from EDX analysis in the transmission electron microscope. The tangential smearing (arc) of the diffraction spots in panels a and b in Figure 7 indicates that the observed spreading is attributed to bending or rotation of atomic planes in the layered structure. It should be noted that the crystallographic orientation of a given set of planes can vary from 0 to 10°,

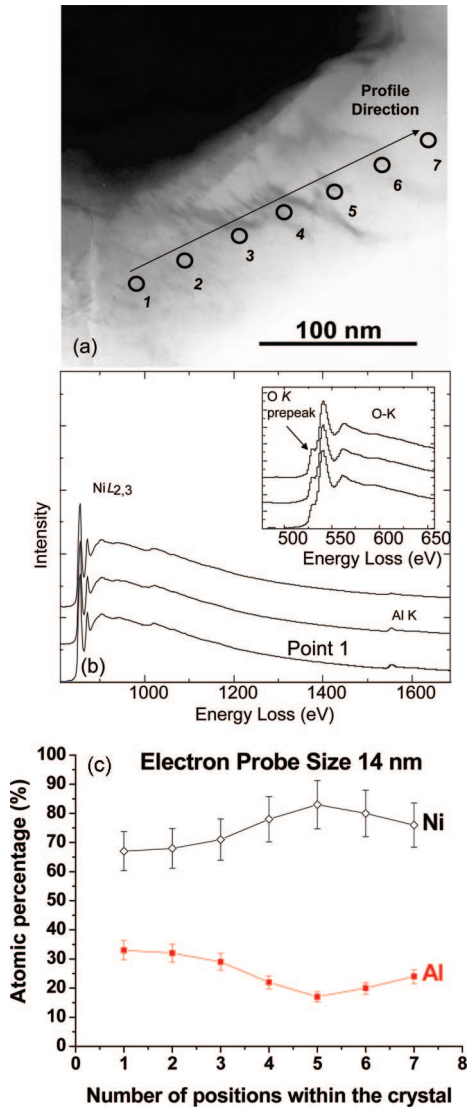

Figure 12. (a) Transmission electron microscope image of another crystal in the "$LiNi_{0.50}Al_{0.50}O_2$" sample, where EELS spectra were collected from 7 different marked locations; (b) EELS spectra of the Ni $L_{2,3}$ and Al K peaks collected from locations 1, 3, and 5 of the crystal shown in (a); (c) relative atomic percentages of nickel and aluminum quantified from the EELS spectra in (b) by comparing the peak intensities of the Ni $L_{2,3}$ and Al K peaks.

such as the (110) planes in Figure 7b. It is believed that the presence of such extensive lattice rotation is a mechanism by which the lattice of "$LiNi_{0.50}Al_{0.50}O_2$" minimizes the overall strain induced by variation in the lattice parameter $a_{hex.}$ associated with nickel and aluminum segregation in the layered structure. Moreover, a careful examination revealed that the radial spreading of the (110) reflections was significantly greater than the $(\bar{1}1\bar{8})$ reflections, which confirmed the presence of considerable anisotropic strains and/or size effect in the (110) planes in the layered structure as shown by synchrotron X-ray powder diffraction analyses. From these electron diffraction pattern an anisotropic strain, $\delta a_{hex.}/a_{hex.}$, of 0.017 was found by considering that only the strains effect was present, which is consistent with the global strains obtained from the refinement results of synchrotron X-ray powder diffraction data (Figure 6).

Convergent beam electron diffraction analysis with an electron beam size on the order of 50 nm revealed reduced lattice rotation in comparison to selected area electron diffraction. A convergent beam and selected area electron diffraction patterns of one crystal in the '$LiNi_{0.50}Al_{0.50}O_2$' sample are shown in a and b in Figure 8, respectively. They are indexed to the [010] zone axis of the layered structure with space group $R\bar{3}m$. No tangential spreading in the electron scattering intensities was observable in the convergent beam electron diffraction pattern in Figure 8a. In contrast, some tangential smearing was found for the (10*l*) planes in the selected area electron diffraction pattern (Figure 8b). This observation suggests that some "$LiNi_{0.50}Al_{0.50}O_2$" crystals consist of nanometer-scale domains (larger than 50 nm for the crystal studied in Figure 8) divided by small angle coherent boundaries, where the lattice rotation and strains are minimized within each domain. It is believed that the presence of these domains at the nanometer-scale is attributed to variation in the nickel and aluminum concentration or segregation of nickel and aluminum in the layered structure. To check that hypothesis, in the following sections we thus analyze the distribution of nickel and aluminum ions within individual crystals on the nanometer-scale in the "$LiNi_{0.50}Al_{0.50}O_2$".

Electron Energy Loss Spectroscopy. EELS was used to probe the chemical inhomogeneity in the nickel and aluminum distribution across different crystals and within individual crystals of the "$LiNi_{0.50}Al_{0.50}O_2$" sample. The relative percentages of nickel and aluminum ions were quantified from the intensities of Ni $L_{2,3}$ and Al K edges, which were obtained from background subtraction and area integration over fixed energy windows. The relative percentages of nickel and aluminum in randomly selected 12 crystals from the "$LiNi_{0.50}Al_{0.50}O_2$" sample calculated from the EELS spectra of the Topcon microscope are shown in Figure 9, respectively. The average nickel and aluminum contents of the "$LiNi_{0.50}Al_{0.50}O_2$" sample obtained from the EELS analysis are consistent with those of EDX (Figure 3). Considerable differences in the nickel and aluminum concentration were found among different crystals and these differences would lead to variation in the lattice parameter $a_{hex.}$ of the layered structure and broadening of all X-ray powder diffraction peaks with nonzero h and k indexes. The results are consistent with the fact that all peaks of the '$LiNi_{1-y}Al_yO_2$' samples were broadened upon aluminum substitution (Figure 1).

In addition to the inhomogeneity among different layered crystals, nickel and aluminum contents were found to vary within individual crystals. A TEM image of a randomly selected single crystal in the "$LiNi_{0.50}Al_{0.50}O_2$" sample is shown in Figure 10, in which the electron diffraction pattern of the crystal is indexed to the $[0\bar{1}0]$ zone axis of the layered structure with space group $R\bar{3}m$ in the insert (bottom left). EELS spectra of Ni $L_{2,3}$ and Al *K* edges collected from different locations along the rod axis of the crystals (from point 1 to point 6 in Figure 10) and the corresponding background subtracted EELS spectra of point 1 and point 6 (normalized at the Ni $L_{2,3}$) are shown in panels a and b of Figure 11, respectively. The dispersion is 2 eV/channel so that the O *K*, Ni $L_{2,3}$, and Al *K* peaks fall within the same measurement (1024 channels are available in the CCD

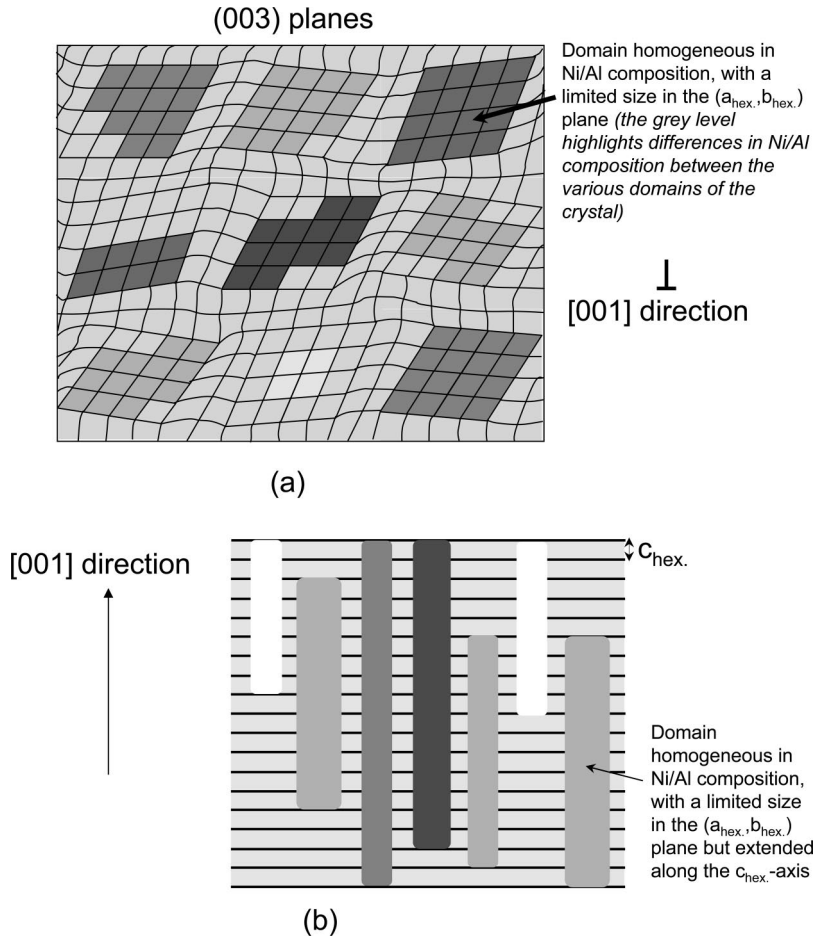

Figure 13. Schematic of the proposed microstructure of the "$LiNi_{0.50}Al_{0.50}O_2$" sample induced by immiscibility of nickel and aluminum ions in the octahedral sites of the layered structure (a) viewed in the basal planes, the (003) planes, and (b) viewed from any directions that lay in the basal plane. Note that variation in the nickel and aluminum concentration could exist in the highly strained regions (highlighted by differences in gray level).

camera). At this dispersion, it should be noted that the prepeak at the O *K* edges is barely visible in the insert of Figure 11a. The relative nickel and aluminum concentrations were quantified from the intensities of the EELS Ni $L_{2,3}$ and Al *K* peaks, as shown in Figure 11c. The nickel and aluminum concentrations were found to vary significantly along the rod axis that lies in the (003) plane of the layered structure. In addition, the slight increase in the intensity of this O *K* prepeak from spot 1 to spot 6 was found. The intensity of the O *K* prepeak arises from the hybridization between the Ni 3d state and the O 2p orbital and the prepeak intensity is directly proportional to the Ni content in the "$LiNi_{1-y}Al_yO_2$" compounds if one assumes an almost constant ionicity of the Ni−O bonding. Therefore, the increase in the intensity of O *K* prepeak is consistent with the increasing Ni/Al ratio from spot 1 to spot 6 shown in Figure 12c. Moreover, it is worthwhile to note that additional EELS spectra (point 7 to point 11 in Figure 10) collected perpendicular to the rod axis showed no variation in the nickel and aluminum content, as shown in Figure 11c.

Inhomogeneous nickel and aluminum distributions on the nanometer-scale within individual crystals were further confirmed by systematic analyses of EELS spectra collected from different locations of other crystals. A TEM image of another randomly selected layered crystal in the "$LiNi_{0.50}Al_{0.50}O_2$" sample and the EELS spectra collected from points 1, 3, and 5 of seven different locations are shown in panels a and b in Figure 12, respectively. Dispersion of the spectrometer was 1.5 eV/ch so that O *K*, Ni $L_{2,3}$, and Al *K* edges were within one measurement, where the visibility of the O *K* pre-edge (Insert in Figure 12a) was improved in comparison to Figure 12a. The quantified nickel and aluminum concentrations from the EELS spectra collected from the crystal in Figure 12a are plotted in Figure 12c. Not only this region had an average chemical composition of $LiNi_{0.75}Al_{0.25}O_2$, significantly different from the nominal chemical composition of the "$LiNi_{0.50}Al_{0.50}O_2$" sample, but also the nickel and aluminum contents were found to vary within this crystal.

Experimental evidence of nickel and aluminum inhomogeneity on the nanometer scale and pronounced peak broadening of (11*l*) type planes in the "$LiNi_{0.50}Al_{0.50}O_2$" sample supports the hypothesis that a complete Li(Ni,Al)O_2 solid solution is thermodynamically unfavorable and miscibility of nickel and aluminum ions in the octahedral sites is limited in the layered structure. Here we propose a domain microstructure for individual "$LiNi_{0.50}Al_{0.50}O_2$" crystals, as shown in Figure 13. Relatively strains-free domains with different nickel and aluminum concentrations coexist with highly strained regions between these domains. It should be noted that variation in the nickel and aluminum concentration

is expected in the highly strained regions (highlighted by differences in gray level).

It is interesting to note that substitution of Co^{3+} and Al^{3+} cations, very similar in charge and in size ($r_i(Co^{3+}) = 0.525$ Å and $r_i(Al^{3+}) = 0.53$ Å), for nickel in $Li(Ni,M)O_2$ rich in Ni^{3+} can lead to random solid solutions for $LiNi_{1-y}Co_yO_2$[21] or to segregation tendency for $LiNi_{1-y}Al_yO_2$. The difference in size between substituted and nickel ions is one critical parameter often used to especially explain the cationic distribution between the lithium and the transition metal layers in the substituted lithium nickel oxides. For example, some of us have discussed in detail the effect of crystal field modified by substitution on the stability of the oxidation state of Ni ions in these layered lithium nickel oxides.[22] Indeed, the distribution of transition metal ions strongly influences the lithium intercalation/deintercalation voltages, structural and thermal stability of these layered structures.[22] In the case of $Li(Ni,Al)O_2$, the difference in size between cations could not explain the segregation tendency between nickel and aluminum, especially because a ramdom solid solution was obtained between cobalt and nickel in $Li(Ni,Co)O_2$. The difference in bond ionicity had to be taken into account; indeed the ionicity of the Al−O bonds is significantly different from that of Ni−O bonds while Co−O bonds have the same ionic character as Ni−O bonds. In our opinion, not only small ionic size difference but also similar ionicity of metal−oxygen bonds is critical to promote complete miscibility of cations in the transition metal layers of the layered lithium transition metal oxides.

Conclusion

Combination of synchrotron X-ray powder diffraction, electron diffraction, and EDX and EELS analyses confirmed the segregation tendency of nickel and aluminum in the layered lithium nickel oxides. This study reveals thus that similar size and charge for the Ni^{3+} and Al^{3+} cations are not sufficient to the achievement of their complete miscibility at the local scale in layered oxide α-$NaFeO_2$-type structure. The similarity in metal−oxygen bonds ionicity appears also critical, first to maintain an almost ideal 2D structure for better lithium diffusion and second to prevent cation segregation which is detrimental to electron mobility in the slabs and thus to lithium diffusion, the two being highly coupled.[23] The characterization of the cation distribution at the local scale in electrode materials is essential as it can affect cycling performance especially at high rates, but probably also chemical stability in the charged state or upon aging. This argument is especially true for layered oxides whose optimized performance in lithium-ion batteries comes from combination of different cations (Ni/Co/Al, Ni/Mn/Co, etc.,) in the same structure.

Acknowledgment. Synchrotron X-ray and electron diffraction data were collected at the European Synchrotron Radiation Facilities (Grenoble, France) and at the Center of Electron Microscopy at Université Bordeaux I, respectively. The authors thank SAFT and Région Aquitaine for financial supports. Y.S.H. acknowledges the support of NSF International Research Fellow Award INT-0000429 and a visiting professorship from Université Bordeaux I.

CM802954G

(21) Saadoune, I.; Ménétrier, M.; Delmas, C. *J. Mater. Chem.* **1997**, *7*, 2505–2511.

(22) Delmas, C.; Ménétrier, M.; Croguennec, L.; Saadoune, I.; Rougier, A.; Pouillerie, C.; Prado, G.; Grüne, M.; Fournès, L. *Electrochim. Acta* **1999**, *45*, 243–253.

(23) Chazel, C.; Ménétrier, M.; Croguennec, L.; Delmas, C. *Inorg. Chem.* **2006**, *45*, 1184–1191, n° 3, p. .